M_3C (M: Fe, Co, Ni) Nanocrystals Encased in Graphene Nanoribbons: An Active and Stable Bifunctional Electrocatalyst for Oxygen Reduction and Hydrogen Evolution Reactions

Xiujun Fan,*,†,‡,§ Zhiwei Peng,‡ Ruquan Ye,‡ Haiqing Zhou,‡,§ and Xia Guo†

†College of Electronic Information and Control Engineering, Beijing University of Technology, Beijing 100124, China and ‡Department of Chemistry, and §Richard E. Smalley Institute for Nanoscale Science and Technology, Rice University, Houston, Texas 77005, United States

ABSTRACT Transition metal carbide nanocrystalline M_3C (M: Fe, Co, Ni) encapsulated in graphitic shells supported with vertically aligned graphene nanoribbons (VA-GNRs) are synthesized through a hot filament chemical vapor deposition (HF-CVD) method. The process is based on the direct reaction between iron group metals (Fe, Co, Ni) and carbon source, which are facilely get high purity carbide nanocrystals (NCs) and avoid any other impurity at relatively low temperature. The M_3C-GNRs exhibit superior enhanced electrocatalystic activity for oxygen reduction reaction (ORR), including low Tafel slope (39, 41, and 45 mV dec^{-1} for Fe_3C-GNRs, Co_3C-GNRs, and Ni_3C-GNRs, respectively), positive onset potential (~0.8 V), high electron transfer number (~4), and long-term stability (no obvious drop after 20 000 s test). The M_3C-GNRs catalyst also exhibits remarkable hydrogen evolution reaction (HER) activity with a large cathodic current density of 166.6, 79.6, and 116.4 mA cm^{-2} at an overpotential of 200 mV, low onset overpotential of 32, 41, and 35 mV, small Tafel slope of 46, 57, and 54 mV dec^{-1} for Fe_3C-GNRs, Co_3C-GNRs, and Ni_3C-GNRs, respectively, as well as an excellent stability in acidic media.

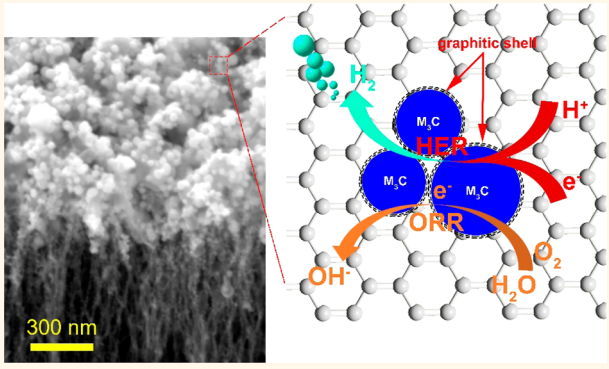

KEYWORDS: oxygen reduction reaction (ORR) · hydrogen evolution reaction (HER) · vertically aligned graphene nanoribbons (VA-GNRs) · M_3C (M: Fe, Co, Ni) · nanocrystals (NCs)

Electrocatalysts for the oxygen reduction (ORR) and hydrogen evolution reaction (HER) are the heart of the key components of fuel cells[1,2] and water splitting,[3] respectively. Pt and its alloys remain the most efficient ORR and HER catalysts,[4,5] but their high cost and scarcity hamper further development of renewable-energy technologies based on these materials. It is therefore attractive to design and synthesize non-Pt-group metal electrocatalysts as alternatives to Pt for ORR and HER, and huge progress has been made in this direction in the past few years. Transition-metal based compounds are an exciting family of such catalysts that have been intensively studied, including MoS_2,[6−8] $CoSe_2$,[9] WS_2,[10] WC,[11] $WS_{2(1-x)}Se_{2x}$,[12] MoB,[13] Mo_2C,[14,15] FeP,[16,17] CoP,[18] Ni_2P[19] and $NiMoN_x$/C.[20] However, most of the reported electrocatalysts toward ORR and HER, such as transition-metal (Co,[21,22] Fe,[23,24] *etc.*), metal oxides (Fe_2O_3,[25] Fe_3O_4,[26,27] Co_3O_4,[28] IrO_2,[29] *etc.*), transition-metal chalcogenides[10,30] are generally prepared in the form of thin films or particle agglomerates coated onto glassy carbon, nickel foam, or other conductive substrates. These well-established non-noble-metal nanocatalysts still require higher overpotential for ORR and HER than Pt. In particular, they show either very limited ORR/HER activity or poor stability in alkaline/acidic solutions. Thus, the development of alternative electrode configurations for efficiently catalyzed ORR and HER with high activity and strong long-term stability is urgently needed.

* Address correspondence to fxiujun@gmail.com.

Received for review April 22, 2015 and accepted June 30, 2015.

Published online June 30, 2015
10.1021/acsnano.5b02420

In this respect, a broad range of alternative catalysts based on nonprecious and earth-abundant iron group transition metal carbides (TMCs, M = Fe, Co and Ni) have garnered much attention due to TMCs exhibiting a catalytic activity similar to Pt-based electrochemical catalysts.[31,32] Nevertheless, it is highly challenging to develop TMCs as efficient multifunctional catalysts for energy conversion system, particularly for unitized regenerative fuel cells and electrolyzers. Many of the well-established routes to metal or metal oxide nanoparticles, such as microemulsion[33] or coprecipitation syntheses,[34] are unsuitable for metal carbide formation. The syntheses of phase-pure Fe_3C, Co_3C and Ni_3C are particularly difficult since the relatively high-temperature and reducing conditions characteristic of many carbide syntheses often result in the formation of metallic iron, cobalt, nickel or mixed M/M_3C (M: Fe, Co, Ni) products.[32,35−38] Alternative synthesis methods have been developed to synthesize phase-pure M_3C (M: Fe, Co, Ni) products, such as spry-pyrolysis,[32,39] sonolysis,[40] or arc-discharge,[41] which lead to agglomerates and polydisperse nanoparticles showing a low electrocatalystic active. However, recently, much attention has been paid to synthesis of hybrid nanostructured of iron group metal carbide (especially Fe_3C) with graphene sheets,[32] CNTs[42] and other mesoporous/macroporous carbon support, which exhibit the promising ORR activity in alkaline media. And carbon-encapsulated TMCs catalysts exhibit better durability for the ORR[31,32] in alkaline media with a controllable number of graphene layers,[43,44] which can efficiently prevent the corrosion of TMCs in harsh condition and simultaneously promote the catalytic reaction on the carbon surface owing to electron penetration from the encapsulated TMCs. Meanwhile, graphene nanoribbons (GNRs) have intrinsic properties, which include high surface area, unique morphology, high electrical conductivity, and their inherent size and hollow geometry can make them extremely attractive as supports for heterogeneous catalysts.[45] Combining porous GNRs with iron group metal carbide nanocrystals (NCs) to form a hybrid may be an effective strategy that integrates their respective merits to enhance the overall catalytic activity. Hence, at this point, there is a need for controllable synthesis of iron group metals carbides NCs supported on GNRs sheets as bifunctional ORR and HER electrocatalyst.

Herein, we report a synthetic strategy that enables facile, economical, and scalable synthesis of vertically aligned graphene nanoribbons (VA-GNRs) supported iron group metals carbides M_3C (M: Fe, Co, Ni) NCs through a hot filament chemical vapor deposition (HF-CVD) method. The obtained M_3C-GNRs exhibited superior enhanced electrocatalystic activity for ORR, including a higher current density, higher electron transfer number (~4), and better durability, potentially making M_3C-GNRs a nonprecious metal cathode catalyst for fuel cells. The M_3C-GNRs (M: Fe, Co, Ni) hybrids exhibit similar ORR catalytic activity but superior stability to Pt in alkaline solutions. The M_3C-GNRs catalyst also exhibit remarkable HER activity with a large cathodic current density of 166.6, 79.6, and 116.4 mA cm^{-2} at overpotential of 200 mV. Moreover, low onset overpotential of 32, 41, and 35 mV and small Tafel slope of 46, 57, and 54 mV dec^{-1} for Fe_3C-GNRs, Co_3C-GNRs, and Ni_3C-GNRs, as well as an excellent stability in acidic media, are achieved. The outstanding activity can be attributed to the sufficiently small size of nanocrystalline M_3C with more active catalytic sites, the synergistic effect between M_3C with graphitic shells and GNRs, favorable charge, and mass transport in the stable M_3C-GNRs hybrid electrode structure.

RESULTS AND DISCUSSION

The fabrication process of M_3C-GNRs (M: Fe, Co, Ni) is illustrated in Figure 1a along with the microscopic characterization data. In the first step, vertically aligned graphene nanoribbons (VA-GNRs) arrays with "teepee" structure were prepared on the Si-wafer with atomic hydrogen treatment (Figure 1b, Supporting Information Figure S1 and S2). This procedure is modified from a previous report.[46] The VA-GNRs (Supporting Information Figure S2) form bundled at the tips, while their bottoms are left at stuck positions on the substrate (Supporting Information Figure S3). Such teepee structure is favorable for depositing metal particles, as the metal particles could easily go through and stay on the tips or side walls of the VA-GNRs, which support the M_3C NCs nucleation and growth. After the deposition of metal M (M: Fe, Co, Ni) onto the teepee structure, carbonization of metal carbide nanoparticles with HF-CVD method was performed at 675 °C (see the Supporting Information for details). Scanning electron microscopy (SEM) observations of M_3C-GNRs also clearly conform that the ordered hybrid structure from the top and channel-like morphology from the cross section are well maintained (Figure 1d, Supporting Information Figure S4). The size and morphology of the M_3C NCs are indicated in Figure 1e−g and Supporting Information Figure S5. The product is composed of a large amount of ultrafine M_3C NCs, and these NCs with irregular shapes are not easily aggregated together. The M_3C NCs are not uniform and most of the NCs have a size smaller than 20 nm. Only a few exceptions with larger grains coexist, which should be due to the aggregation and growth under the carbonization process. Notably, except of a few of the larger M_3C NCs at the top of VA-GNRs that are not connected to the GNRs, most of ultrafine M_3C NCs are inlaid into GNRs support, which also act as bridges to connect the M_3C NCs, thereby enhancing the overall electron transfer capability. The temperature used for CVD growth of M_3C NCs here (675 °C) is much lower than that conventionally used (800−1000 °C with iron

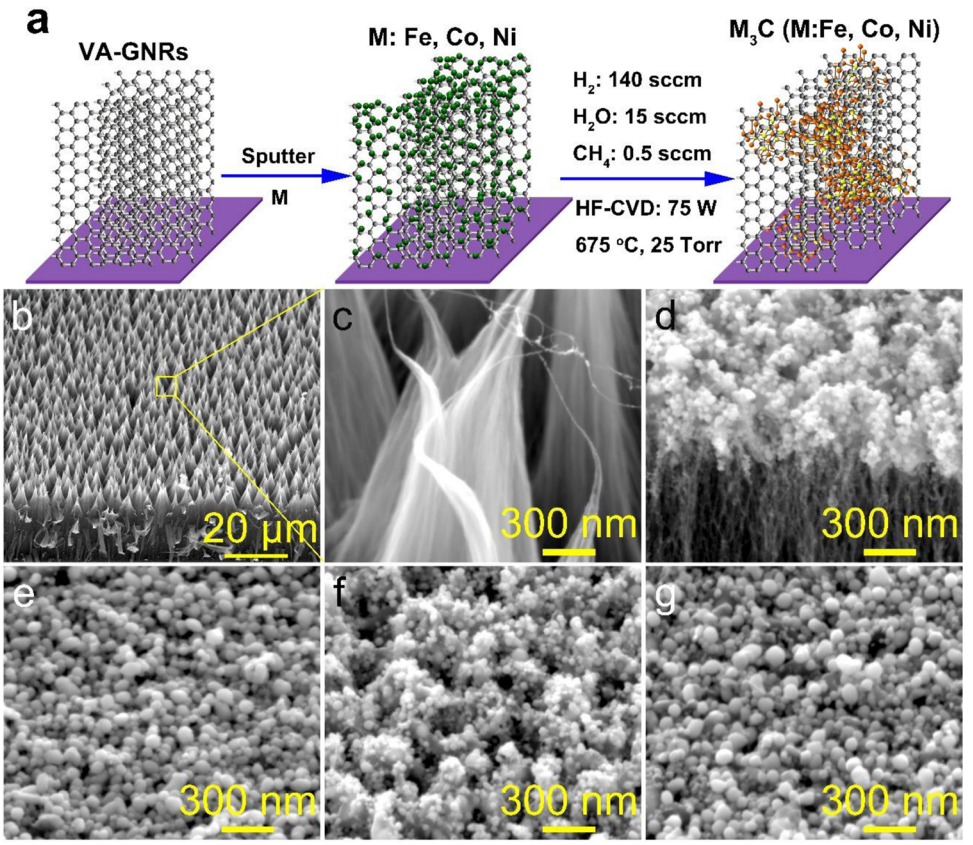

Figure 1. (a) Schematic illustration of the formation mechanism of nanocrystalline M_3C (M: Fe, Co, Ni) on VA-GNRs. (b and c) SEM images of VA-GNRs with "teepee" structure. (d) Typical SEM image of M_3C-GNRs; (e−g) SEM images of M_3C (M: Fe, Co, Ni) NCs grown on the tips of VA-GNRs.

particles as catalyst).[47] This is likely due to (1) the nanoporous structures of VA-GNRs that enable faster diffusion and better dissolution of carbon through their ordered channels (Figure 1b,c); (2) the HF-CVD process.[48]

The X-ray diffraction (XRD) pattern for the product corresponded well with that expected for nanocrystalline M_3C (M: Fe, Co, Ni) (Figure 2a). Typical strong peaks at about 26° are observed, corresponding to the (002) facets of graphite carbon, in agreement with the structural feature of GNRs. As exhibited in bottom curve in Figure 2a, the peaks located at 37.8, 43.9, 45.0, 46.0, 49.2, and 54.5° correspond to the Fe_3C (JCPDS 35-0772). The middle curve in Figure 2a reveals the XRD pattern of the as-synthesized Co_3C NCs, which can be indexed to Co_3C (JCPDS 89-2866) with space group *Pnma* (a = 0.508 nm, b = 0.673 nm and c = 0.452 nm). As revealed in the top curve in Figure 2a, the small reflection peaks visible at 39.31, 41.81, 45.02, and 58.71, corresponding to the (100), (002), (101), and (102) reflections of the crystalline planes of Ni_3C species, respectively. These XRD results indicate that the product of M_3C-GNRs is a mixture of two phases: graphite carbon and M_3C. The M_3C content and graphitic qualities of the as-synthesized M_3C-GNRs are evaluated through thermogravimetric analysis (TGA) and Raman spectroscopy techniques. As revealed in Figure 2b, for M_3C-GNRs, no significant weight loss is detected below 500 °C. Above 500 °C, the decrease in weight starts and continues until 645 °C, then remains stable up to 850 °C. The most remainder in M_3C-GNRs is presumably from the remaining M_3C. The VA-GNRs display a negligible amount of residual weight (0.3 wt %) up to 850 °C in air. Considering the amount of residual weight for VA-GNRs is small, the M_3C amount for Fe_3C-GNRs, Co_3C-GNRs, and Ni_3C-GNRs can determined to be ~18.26, 24.63, and 18.25 wt %, respectively. Raman spectra are used to study the degree of graphitization of the M_3C-GNRs samples because the D band (1360 cm^{-1}) and G band (1590 cm^{-1}) provide information on the disorder and crystallinity of sp^2 carbon materials, respectively. After being hybridized with M_3C, the I_G/I_D of M_3C-GNRs is largely increased (Figure 2c), indicating the graphitic structure of GNRs is greatly enhanced; this should be ascribed to the catalytic graphitization effect.[49] The more perfect crystalline structure is in favor of improving the electrical conductivity.[42] The obvious upshift of 2D band in comparison with that of VA-GNRs may be due to the existence of carbon shells in M_3C-GNRs hybrids. Additionally, compared with Raman spectra of M@ VA-GNRs (M metallic particles on the top of VA-GNRs, M: Fe, Co, Ni) (Supporting Information Figure S6), the absence of the Raman peaks at low Raman shift ranged from

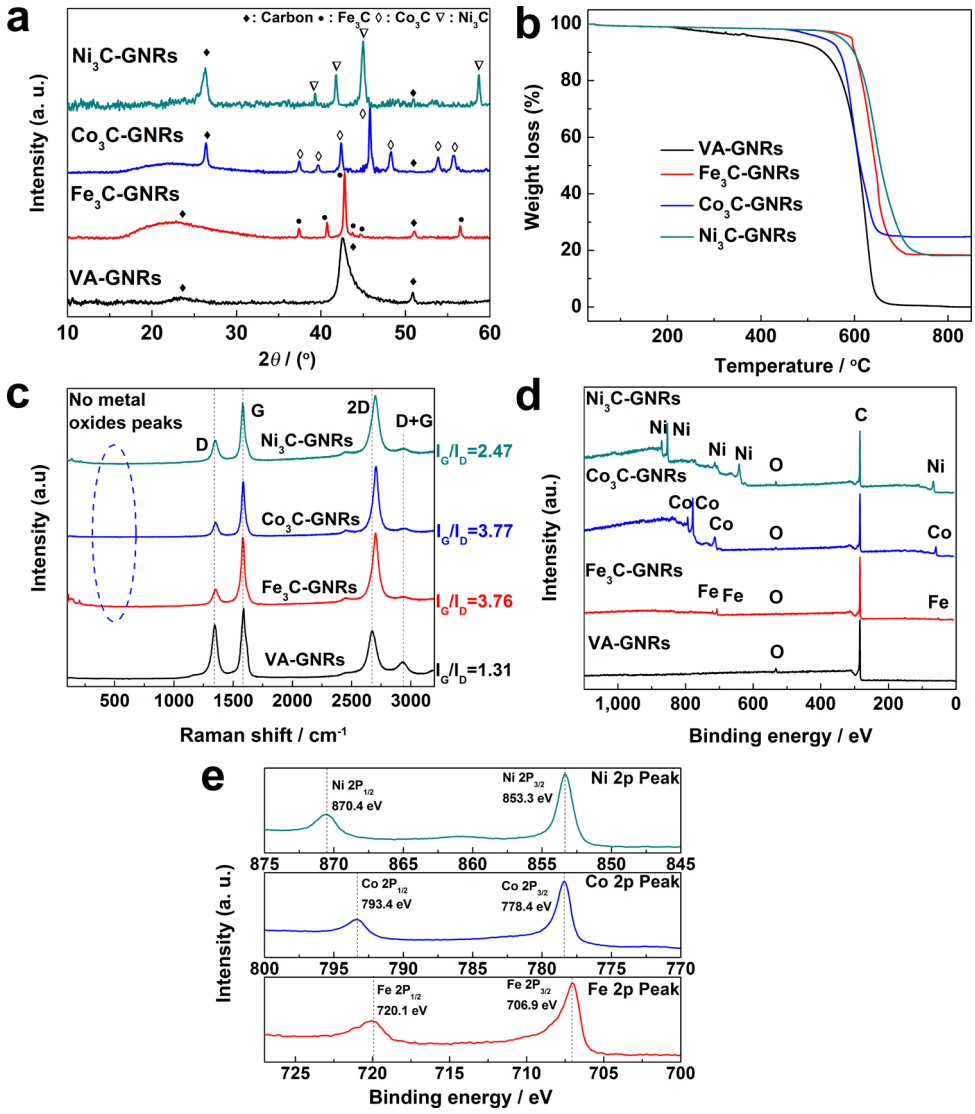

Figure 2. (a) XRD patterns for M_3C NCs grown on VA-GNRs, indicating that carbonous and carbides phases have been identified, respectively. (b) TGA thermograms obtained from the heating rate 5 °C min^{-1} in air. (c) The Raman spectra of VA-GNRs and M_3C-GNRs (M: Fe, Co, Ni). (d) XPS survey spectra of VA-GNRs and M_3C-GNRs; (e) M2p (M: Fe, Co, Ni) XPS spectrum of M_3C-GNRs.

100 to 750 cm^{-1}, indicates that metal oxides are totally transformed into metal carbide with HF-CVD process. The X-ray photoelectron spectroscopy (XPS) spectroscopy was also conducted to identify the surface nature of the M_3C NCs. The survey XPS spectrum of M_3C-GNRs (Figure 2d) reveals that M_3C-GNRs are composed of C, O, and M (M: Fe, Co, Ni), and no other impurity is observed, which is consistent with the results of XRD. The widths of the C 1s peaks at ~284.5 eV in the C 1s spectrum become smaller as the HF-CVD process, suggesting enhanced graphitization with atomic hydrogen treatment (Supporting Information Figure S7).[50] The two peaks at ~707.0 and ~720.1 eV in the Fe 2p spectrum of Fe_3C-GNRs (top in Figure 2e) can be assigned to Fe_3C. Furthermore, peaks at 793.3 and 778.4 eV turn up, indicating the main component is Co_3C (middle in Figure 2e). The peaks at 870.5 and 853.3 eV in the Ni 2p XPS spectrum suggest the existence the carbide phase in the carbon composite, also demonstrate the existence of Ni_3C (bottom in Figure 2e). We have noticed the fact that XPS signals are very strong; such high metal surface contents imply that the M_3C nanoparticles are exclusively encased by few carbon layers in the NCs. The M_3C (M: Fe, Co, Ni) NCs are synthesized by one-step carbonization directly using metal M (M: Fe, Co, Ni) as precursors. The synthesis is facile and cheap, a high reproducibility in terms of structure and performance.

The size and crystal structure of M_3C-GNRs products were further examined with transmission electron microscopy (TEM). Figure 3a displays a typical TEM image of the Fe_3C-GNRs. Fe_3C NCs are dispersed in carbon matrix with different shapes, such as spheres, ellipsoids, hexagons, *etc*. It can be seen from the particle size distribution

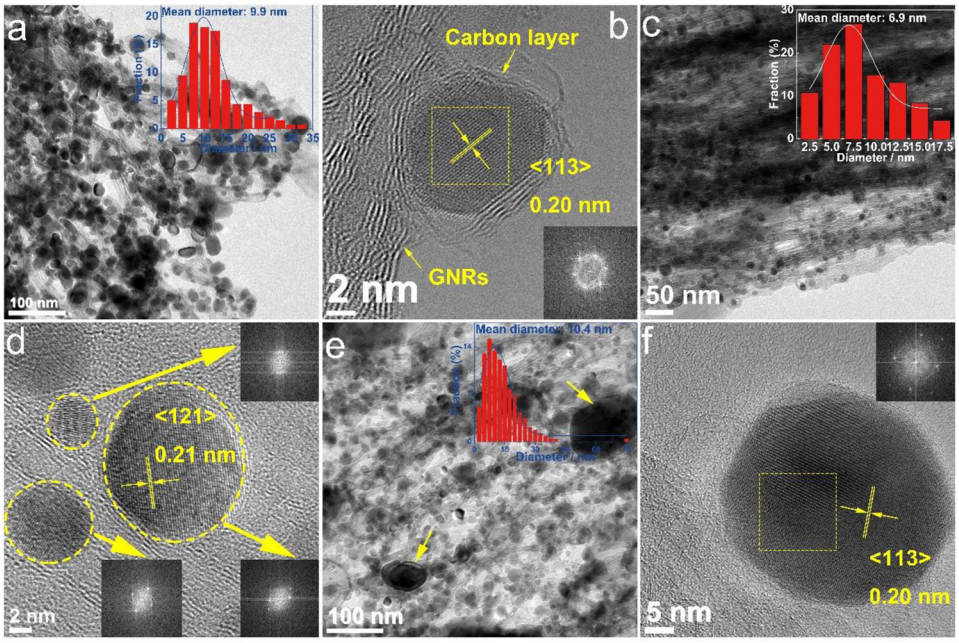

Figure 3. TEM and high-resolution TEM images of carbon-encapsulated M_3C NCs grown at 675 °C for 3 h. (a and b) Fe_3C-GNRs, (c and d) Co_3C-GNRs, (e and f) Ni_3C-GNRs. The insets in (a), (c), and (e) are corresponding particle size distributions of the M_3C. The fast Fourier transform (FFT) patterns taken from selected area in (b), (d), and (f) are employed to verify the nanocrystlline M_3C structure.

shown in the inset of Figure 3a that the diameters of the particles varied from 2.5 to 32.5 nm with the average diameter of ~9.9 nm. The high-resolution transmission electron microscopy (HRTEM) image of the NCs is seen in Figure 3b, and the interlayer spacing value of metal carbide is about 0.20 nm, which is in accordance with the value of d_{103} of Fe_3C, indicating Fe_3C is the main nanometal type in this Fe/C system. Surrounding the Fe_3C NCs, the carbon layers with well-ordered arrangement are closely compacted forming the graphite shells (or quasi-nano-onion) structure,[51] which are of importance for mass transport in electrocatalytic performance for ORR and HER. Supporting Information Figure S8a depicts a nanoparticle with a closed shell, and well-defined crystalline lattice spacing of 0.24 nm can be observed in the core, which is consistent with the (210) diffraction peak of Fe_3C. On the basis of the TEM analysis, it is apparent that Fe/FeO_x is totally transformed into Fe_3C coating of few layer graphite shells. Figure 3c-d present the structure of the typical catalyst Co_3C-GNRs. The Co_3C NCs are significantly more uniform than the Fe_3C NCs. The characteristic morphology is dimensionally uniform spheres with a diameter of 2.5−17.5 nm. Graphite shells around the spheres-liked Co_3C nanoparticle can be easily identified, as seen in Figure 3d and Supporting Information Figure S8b. The lattice spacing in the core is 0.21 nm, corresponding to the (121) plane of Co_3C, while the shell structure appeared to be few layer graphene. TEM images show that most of the synthesized Ni_3C NCs are spherical with the average diameter of ~10.4 nm (Figure 3e and Supporting Information Figure S8c), except a few abnormally large particles (indicated with yellow arrows). Close observation further reveals that Ni_3C NCs uniformly dispersed in the sphere structure (Figure 3f). The three- to four-layer graphite shells coated on the surface of the Ni_3C NCs are identified from the typical 0.34 nm *d*-spacing that corresponds to the C (002) plane as indicated by the lattice fringes (Supporting Information Figure S8c). Overall, except of a few large particles, most M_3C NCs with small size are uniformly decorated on GNRs without detachment and aggregation. Although these metal particles are prepared under the same processing conditions, the size of the formed particles differs with respect to the type of elements, which means the properties of the elements themselves such as the differences in melting points or vapor pressures may play a role in size variations.[52] For catalysts and other materials prepared by pyrolysis, structure control is always a difficult task,[53] and this is particularly true for preparation of iron group metals carbides. On the basis of the above results, it could be firmly concluded that HF-CVD is an efficiently way to synthesize homogeneously dispersed and well-interacting nanocrystalline M_3C and conductive carbon species in M_3C-GNRs, which is desired for high-performance electrocatalysts.

To gain insight into the ORR activity of M_3C-GNRs, we first examined the electrocatalystic properties of M_3C-GNRs in a Ar- and O_2-saturated 0.1 M aqueous KOH electrolyte solution using cyclivoltammetry at a scan rate of 5 mV s^{-1} (Figure 4a) (see the Supporting Information for experimental details). The VA-GNRs (free of M_3C NCs) exhibit very poor ORR activity (Supporting Information Figure S9). Remarkably, the M_3C-GNRs

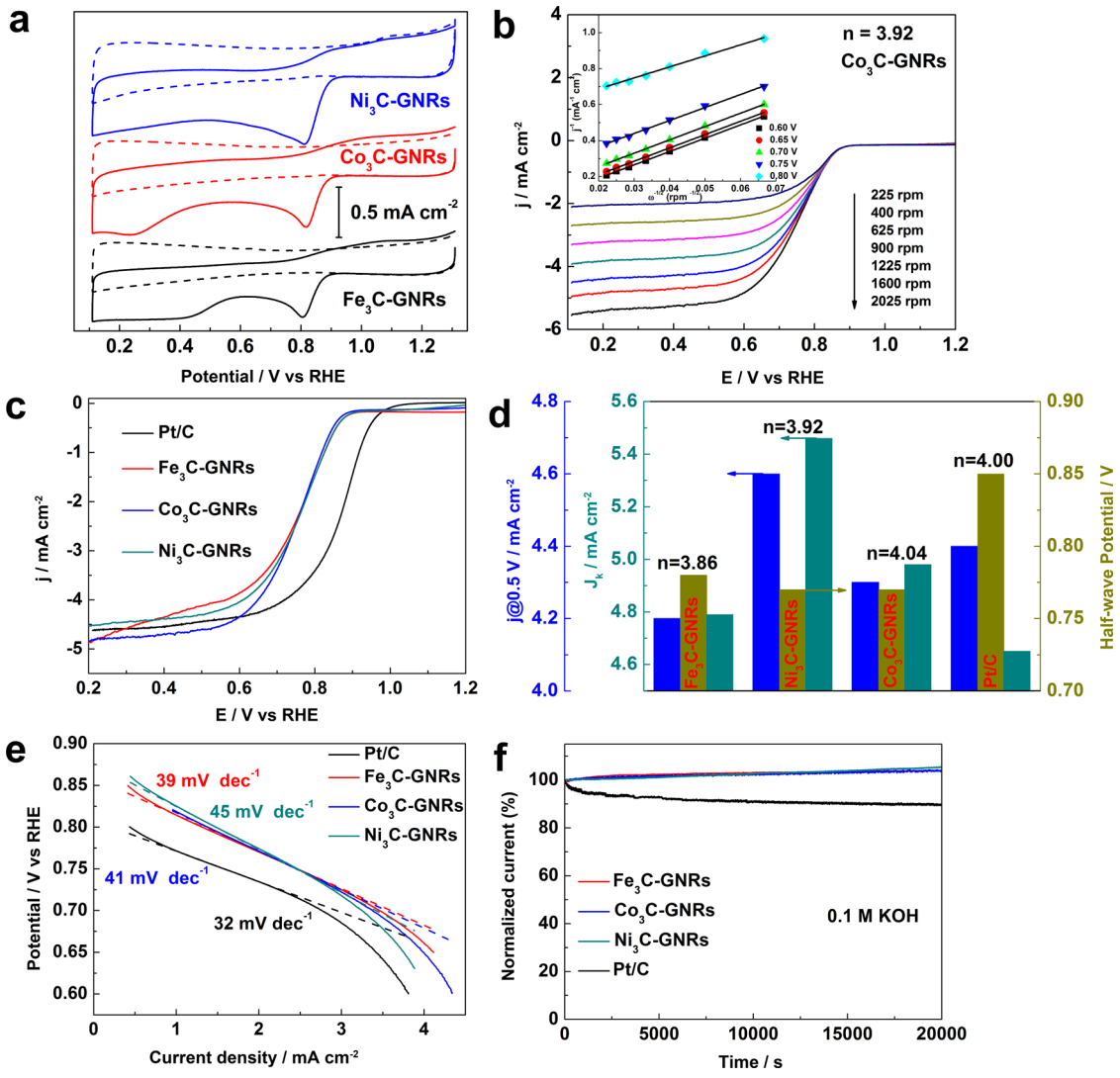

Figure 4. (a) CVs of M_3C-GNRs (M: Fe, Co, Ni) in Ar- and O_2 -saturated 0.1 M aqueous KOH electrolyte solutions at a scan rate of 5 mV s^{-1}. (b) RDE LSVs of ORR on Co_3C-GNRs in O_2-saturated 0.1 M KOH at a scan rate of 5 mV s^{-1}; inset shows corresponding Koutecky−Levich plots (J^{-1} *versus* rpm $^{-1/2}$) at different potentials. (c) LSV curves of M_3C-GNRs (M: Fe, Co, Ni) and Pt/C at a rotation rate of 1600 rpm in O_2-saturated 0.1 M KOH solution. (d) The corresponding *j*@0.5 V *vs* RHE, half-wave potentials and J_k of M_3C-GNRs (M: Fe, Co, Ni) and Pt/C, *j*@0.5 V measured at 1600 rpm. (e) Tafel plots of M_3C-GNRs (M: Fe, Co, Ni) electrocatalyst derived by the corresponding RDE data (see Supporting Information). (f) The relative ORR cathodic current−time response (1600 rpm) at M_3C-GNRs (M: Fe, Co, Ni) and Pt/C (20%) electrodes at −0.5 V in O_2 saturated 0.1 M KOH for 20 000 s.

hybrids afford a much more positive ORR onset potential and peak potential (~0.95 and 0.82 V *vs* the reversible hydrogen electrode (RHE), respectively), and it is convincing that the M_3C (M: Fe, Co, Ni) NCs play a key role in improving the catalytic performance for ORR (Supporting Information Table S1). The GNRs can not only hamper the aggregation of M_3C (M: Fe, Co, Ni) NCs but also serve as a conduction path for shuttling electrons toward ORR. This suggested that similar to the Co_3O_4/N-rmGO case,[28] the high catalytic activity of M_3C-GNRs is facilitated by the strong coupling between M_3C (M: Fe, Co, Ni) NCs and GNRs. This can be further confirmed by electrochemical impedance spectroscopy (EIS) characterization (Figure S10, Supporting Information). The hybrid exhibits a much lower charge transfer resistance (R_{CT}) as compared with VA-GNRs, suggesting that more effective shuttling of charges between the electrode and the electrolyte occurs at the hybrid interface. The above results suggest that the high catalytic performance of M_3C-GNRs is probably attributed to the coexistence of GNRs and M_3C species, which are the active sites for ORR. The GNRs serve as "highways" for electron transport, and the M_3C NCs covered with graphitic shell facilitate direct electrical contacts between neighboring GNRs in the composite, providing an efficient electron transport network and thus promoting electron transport in the composite catalyst. To understand the key ORR electrocatalytic activity in M_3C-GNRs hybrids, linear sweep voltammograms (LSVs) were recorded in an O_2-saturated 0.1 M

KOH electrolyte at a scan rate of 5 mV s^{-1} using a rotating disk electrode (RDE) (Figure 4b, and Supporting Information Figure S11). The electron transfer number (n) and the kinetic-limiting current density (J_k), two important parameters that reflect the kinetics of ORR process, are calculated from the slope and the reciprocal of the intercept of the K–L plots, respectively (see Methods section for the details of the calculation of J_k and n).The reaction transfer numbers (n) are calculated to ~3.9 at 0.6–0.8 V from the slope of Koutecky–Levich plots, indicating that ORR at M_3C-GNRs electrodes proceeds by an approximate four-electron reduction pathway, corresponding to the complete reduction of oxygen into water.[54] The half-wave potentials at 1600 rpm are 0.78, 0.77, and 0.77 V for Fe_3C-GNRs, Co_3C-GNRs, and Ni_3C-GNRs, respectively (Figure 4c,d), close to that of Pt/C (0.85 V; Supporting Information Figure S12). Impressively, the J_k values of the hybrid are all slightly higher than those of the commercial Pt/C catalyst, and their j@0.5 V values are close to those of Pt/C (Figure 4d). The high current density of M_3C-GNRs hybrids should be derived from the unique morphological and structural characteristics of M_3C-GNRs hybrids, including being highly active M_3C NCs with a small size, and the heterojunction at the interface between M_3C (M: Fe, Co, Ni) NCs and GNRs sheets. Excellent ORR activity of the M_3C-GNRs hybrid catalyst is also gleaned from the much smaller Tafel slopes at low overpotentials (39, 41, and 45 mV dec^{-1} for Fe_3C-GNRs, Co_3C-GNRs, and Ni_3C-GNRs, respectively) (Figure 4e), which are close to that of Pt/C (32 mV dec^{-1}) measured in 0.1 M KOH. Therefore, similar to the ORR processes on Pt/C catalyst in alkaline media, transfer of the first electron is the rate-determining step of the ORR for the M_3C-GNRs catalysts.[31] All these results demonstrate that M_3C-GNRs are indeed highly efficient ORR electrocatalysts. To investigate the stability of M_3C-GNRs electrode toward ORR, the chronoamperometric tests of M_3C-GNRs and Pt/C (20%) electrodes were performed at −0.5 V in O_2-saturated 0.1 M KOH (Figure 4f). No obvious loss of current density happens along with the increasing time for M_3C-GNRs, indicating the catalytically active phase remained intact during the alkaline leaching process. In contrast, the current density of Pt/C decreases continuously with 88% retention. This confirms the much better stability of M_3C-GNRs (M: Fe, Co, Ni) than that of Pt/C. The role of metal carbide (especially, Fe_3C) phase in the ORR has been a long-term debated topic in terms of whether Fe_3C is necessary for improving the activity or nitrogen can do it by itself. This is because of two reasons: (1) the prepared Fe_3C-based catalysts were found to contain a certain amount of surface nitrogen, indicating the possible presence of Fe_xN or/and N_xC sites; (2) reported catalysts were a mixture of several phases, for example, carbon-coated Fe_3C in different scales, bare Fe_3C, and metallic Fe particles, making it difficult to conclude the role of the Fe_3C phase in the ORR.[31] In our case, the M_3C-GNRs (M: Fe, Co, Ni) are prepared using pure metal (M: Fe, Co, Ni) as precursors and the obtained catalyst do not contain any amount of nitrogen or other phase such as metallic M (M: Fe, Co, Ni) particles. Thus, it is reasonable to deduce that there is only one type of active sites in the hybrid: M_3C (M: Fe, Co, Ni) NCs. We attribute the high active and stability to the coupling effect between M_3C NCs and GNRs.

Now, that the as-prepared M_3C-GNRs (M: Fe, Co, Ni) demonstrated great ORR performance, how about their HER activity? The HER activity of the catalysts are evaluated in a typical three-electrode cell setup with 0.5 M H_2SO_4 electrolyte (see the Methods section). For comparison, bare VA-GNRs and commercial Pt wire were also examined. As displayed in Figure 5a, VA-GNRs alone show very poor HER performance. M_3C-GNRs hybrids exhibit significantly higher activity than those of VA-GNRs, benefiting from M_3C NCs in M_3C-GNRs hybrids. The overpotentials required to drive cathodic current density of 10 mA cm^{-2} are 49, 91, and 48 mV for Fe_3C-GNRs, Co_3C-GNRs, and Ni_3C-GNRs, respectively. These overpotentials are among the most active for the electrocatalysts based on non-noble materials (see Supporting Information Table S1). Tafel plots are shown in Figure 5b. These Tafel plots were fit to the Tafel equation ($\eta = b \log j + a$, where j is the current density and b is the Tafel slope), yielding Tafel slopes of approximately 46, 57, and 54 mV dec^{-1} for Fe_3C-GNRs, Co_3C-GNRs, and Ni_3C-GNRs electrodes, respectively. This suggests that the HER occurs through a Volmer–Heyrovsky mechanism, in which a fast discharge of a proton is followed by rate limiting electrochemical recombination with an additional proton.[8] The small Tafel slope for M_3C-GNRs catalyst observed here is desirable to drive a large catalytic current density at low overpotential. This demonstrates that M_3C-GNRs have a comparable HER activity to the commercial Pt catalyst. The capacitance is proportional to the contact area between the catalysts and electrolyte. In electrocatalysis, high contact area is favorable for high activity. The capacitance of the double layer at the solid–liquid interface with cyclic voltammetry was measured in Figure 5c and Supporting Information Figure S13 to estimate the effective surface areas. The halves of the positive and negative current density differences at the center of the scanning potential ranges are plotted *versus* the voltage scan rates in Figure 5d, in which the slopes are the electrochemical double-layer capacitances. The capacitance of Fe_3C-GNRs, Co_3C-GNRs, and Ni_3C-GNRs are 25.4, 21.6, and 23.7 mF cm^{-2}, respectively. In contrast, the capacitance of smooth M_3C is 22 μF cm^{-2}, within the typical range for a flat electrode.[55] Accordingly, the roughness factor of Fe_3C-GNRs, Co_3C-GNRs, and Ni_3C-GNRs are 1154.5, 981.8, and 1077.2, respectively. The electrochemical surface area serves as an approximate guide for surface

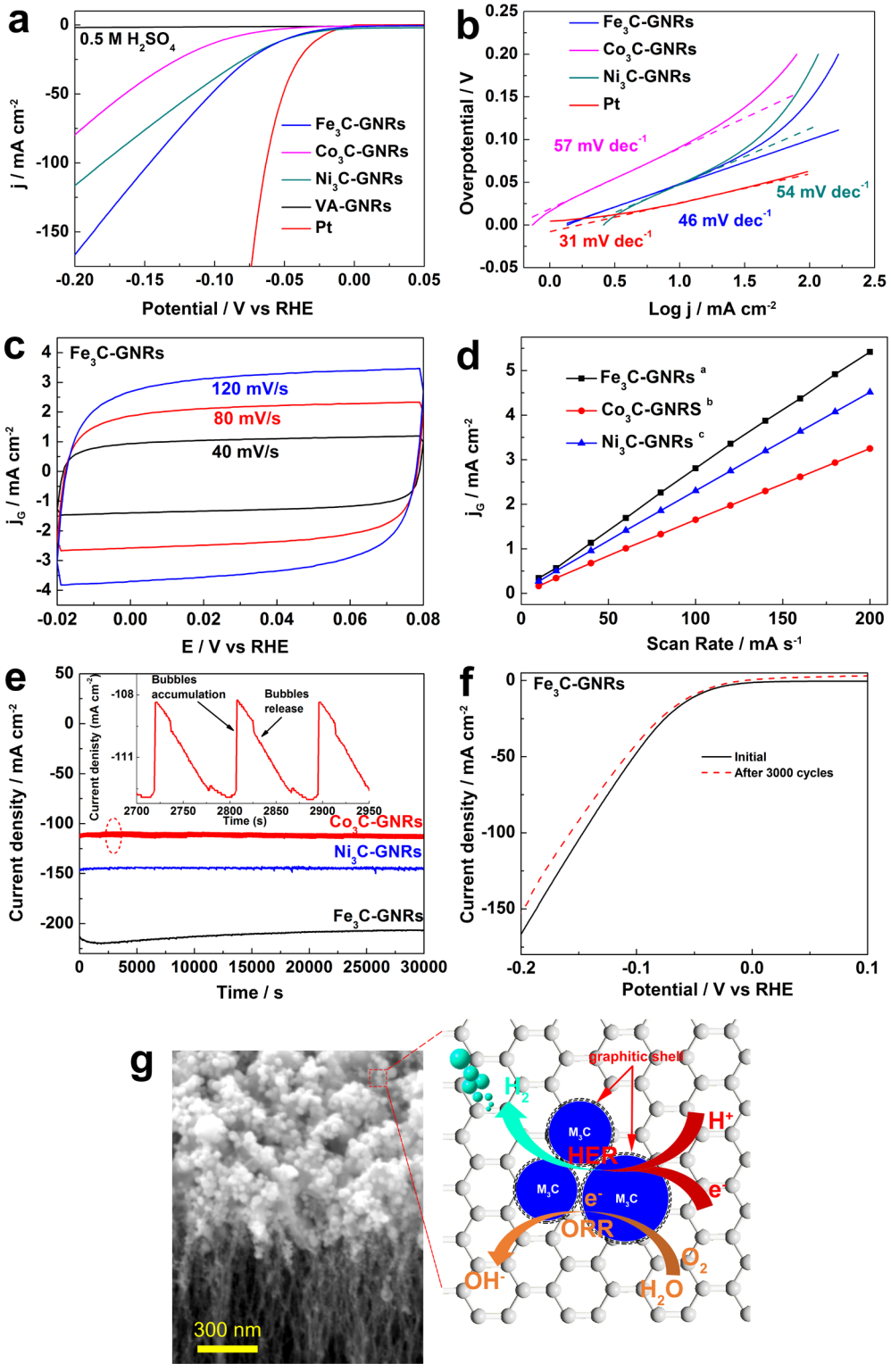

Figure 5. (a) Polarization curves of M_3C-GNRs (M: Fe, Co, Ni) electrode in 0.5 M H_2SO_4, along with VA-GNRs, and Pt wire for comparison. (b) Corresponding Tafel plots in comparison with a Pt wire. (c) Cyclic voltammograms (CV) are taken in a potential window without faradaic processes. (d) The capacitive currents as a function of scan rate for M_3C-GNRs (M: Fe, Co, Ni) electrodes. (a, b, and c are measured at 0.03, 0.01, and −0.05 V *vs* RHE, respectively). (e) Time dependence of current static overpotential of 235 mV. Inset: enlargement of the area denoted by the dash circle. (f) Polarization curves for Fe_3C-GNRs at a scan rate of 50 mV s^{-1} before and after 3000 cycles at a scan rate of 50 mV between +0.1 and −0.2 V *vs* RHE. (g) Mechanism diagram of catalytic reaction for M_3C-GNRs (M: Fe, Co, Ni) electrodes.

roughness within an order-of-magnitude accuracy. Therefore, the active overall HER activity of the M_3C-GNRs (M: Fe, Co, Ni) electrode is associated with its high surface area. First, the small size of the

M_3C NCs in the hybrid favors the exposure of more active sites for the HER. Second, the excellent electrical conductivity of the GNRs support facilitates charge transfer in the hybrid. Indeed, electrochemical impedance spectroscopy measurements indicate that M_3C-GNRs have a much lower impedance and thus markedly faster HER kinetics (Supporting Information Figure S14).

Stability is another significant criterion by which to evaluate a HER catalyst. To probe the durability of the M_3C-GNRs in an acidic environment, continuous HER at static overpotential and a long-term cycling test were conducted. At first, the practical operation of the catalyst is examined by electrolysis at fixed potentials over extended periods. As demonstrated in Figure 5e, at a static overpotential of 235 mV, the catalyst current density of Co_3C-GNRs and Ni_3C-GNRs electrode remains stable at approximately -111 and -147 mA/cm^2 for electrolysis over 30 000 s. For Fe_3C-GNRs electrode, a little increase in cathodic current density of less than 10% is observed during the first 1 h; then the current density exhibits only slight degradation even after a long period of 30 000 s, which might be caused by the consumption of H^+ or the remaining of H_2 bubbles on the surface of the electrode that hindered the reaction. The as-measured time-dependent curve is in typical serrate shape, which can be attributed to the alternate processes of bubble accumulation and bubble release (inset in Figure 5e).[30] This exceptional durability shows promise for practical applications of the catalysts over the long-term. A long-term cycling test was also performed by taking continuous cyclic voltammograms at an accelerated scanning rate of 50 mV s^{-1} for 3000 cycles. Figure 5f displays the comparison of $I-V$ curves measured before and after 3000 CV cycles ranging from 0.1 to -0.2 V *vs* RHE for Fe_3C-GNRs. The negligible difference in the curves also indicates that the Fe_3C-GNRs catalysts are of superior stability in a long-term electrochemical process. As shown in Supporting Information Figure S15, the polarization curves of Co_3C-GNRs and Ni_3C-GNRs catalysts after 3000 cycles both overlay almost exactly with the initial one, with negligible loss of cathodic current. This confirms the M_3C-GNRs (M: Fe, Co, Ni) catalysts are highly stable to withstand accelerated degradation. The XPS spectra of the sample after the HER process for 30 000 s show negligible change of the oxidation state for M (M: Fe, Co and Ni), which confirms the excellent stability of the NCs under the long-term electrochemical cycling process (Supporting Information Figure S16). The high performance and stability of M_3C-GNRs hybrid catalyst in HER are attributed to the small NCs size, relative uniformly distribution, accordingly highly electronic conductivity and high surface area.

The mechanism of M_3C-GNRs hybrid catalyst for ORR and HER has been proposed. The GNRs support substantially increased the conductivity of the synthesized catalysts, provided high surface area to contact with electrolyte, and dispersed the M_3C NCs without aggregation.[13] The high activity and excellent stability of the prepared M_3C-GNRs (M: Fe, Co, Ni) can be attributed to three aspects: (i) The GNRs with unique 1D structure not only provide highly active hydrogen binding sites during the HER process, but also facilitate interelectron transport along the basal surfaces of M_3C-GNRs (Figure 5g). (ii) The anchored configuration of M_3C-GNRs (M: Fe, Co, Ni) induces a unique host–guest electronic interaction and changes the local work function of the graphene sheet, making the surface of the carbon layer more active to ORR; this close interconnection between M_3C and carbon species hampers the aggregation of M_3C NCs and provides a resistance-less path suitable for fast electron transfer, thereby facilitating highly reactive sites on the surfaces. (iii) The disordered distribution of the M_3C on GNRs, just like "islands" covered in graphene sheets, can improve bubble convection and release away from the electrode surface preventing the H_2(g) bubbles from damaging the catalysts during the accumulation process, thus leading to a much long-term stability of M_3C-GNRs (M: Fe, Co, Ni) electrodes. Due to the high quality, small size of M_3C NCs grown on VA-GNRs, the high electrochemical surface area, and the synergistic effect between M_3C and GNRs, the M_3C-GNRs hybrid also gives high ORR activity. In general, the unique 3D assembled architecture of 1D M_3C combined with 2D graphene sheets provides a new nonprecious metal catalyst for highly efficient electrocatalytic oxygen reduction and hydrogen evolution reactions.

CONCLUSION

In summary, the synthesis of iron group metal carbide M_3C (M: Fe, Co, Ni) nanocrystals embedded on VA-GNRs has been effectively prepared using HF-CVD method. The physiochemical characterization including SEM, XRD and TEM investigation verifies that the high purity M_3C NCs are well anchored on M_3C-GNRs (M: Fe, Co, Ni) hybrid, revealing the effectiveness of synthesis method. Due to the sufficiently small size of M_3C NCs with more active catalytic sites and microporous structure of M_3C-GNRs, the resulting hybrids show excellent electrocatalytic activity for the ORR in alkaline electrolytes and HER in acidic media. The M_3C-GNRs exhibit greatly enhanced electrocatalystic activity for ORR, including a higher current density, higher electron transfer number (~4), and stronger durability, potentially making M_3C-GNRs a nonprecious metal cathode catalyst for fuel cells. The M_3C-GNRs catalysts also exhibit remarkable HER activity with a large cathodic current density of 166.6, 79.6, and 116.4 mA cm^{-2} at an overpotential of -200 mV,

low onset overpotential of 32, 41, and 35 mV, and small Tafel slope of 46, 57, and 54 mV dec^{-1} for Fe_3C-GNRs, Co_3C-GNRs, and Ni_3C-GNRs, respectively, associated with long-term stability achieved, making M_3C-GNRs (M: Fe, Co, Ni) catalysts a promising alternative nonprecious HER electrocatalyst.

METHODS

Synthesis of VA-GNRs Carpets through VA-CNTs. Vertically aligned graphene nanoribbons (VA-GNRs) with teepee structure were prepared with atomic hydrogen treatment process described in detail elsewhere.[46] Vertically aligned carbon nanotubes (VA-CNTs) arrays were first grown in a standard water-assisted chemical vapor deposition process. Then, the VA-CNTs carpet samples were loaded into the CVD furnace chamber below the hot filament and treated with atomic H. Typically, atomic H treatment was carried out using a mixture of H_2 (140 sccm), H_2O (15 sccm) and CH_4 (0.1 sccm) at 25 Torr at 850 °C for 0.5 h to unzip VA-CNTs and form VA-GNRs. The filament is ~8 mm long and made from 0.25 mm tungsten wire. And 4 tungsten wires were used to make a filament array assembly. The hot filament power was keep at 65 W.

M_3C (M: Fe, Co, Ni) Nanocrystals Synthesis on VA-GNRs. In a typical synthesis, a layer of metal M (M: Fe, Co, Ni) 10−150 nm was deposited on the tips of VA-GNRs with sputter or electron beam system. The VA-GNRs carpets with a layer of metal were loaded into the CVD furnace chamber below the hot filament about 3−6 mm do the treatment the same as grown VA-GNRs at 675 °C for 3−9 h. After growth, the M_3C-GNRs (M: Fe, Co, Ni) were detached from the Si wafer simply by peeling off from the Si substrate using a blade.

General Materials Characterization. A Bruker D_8 Advance diffractometer (DMAX 2500) operating with a Cu Kα energy source at 40 kV and 40 mA was used to crystallographically characterize the materials. The XPS spectra were calibrated against the carbon 1s photoelectron signal at 284.5 eV on an Amicus/ESCA 3400 from Kratos Analytical instrument operating with dual Mg/Al anodes with an energy source at 12 kV and 10 mA. TGA was performed in a Mettler-Toledo TGA/DSC1 Star system under air (100 mL min^{-1}). The Brunauer−Emmett−Teller (BET) surface area was measured on a Quantachrome autosorb-3b BET surface analyzer. A field-emission TEM (JEOL 2010F) with an imaging filter (Gatan GIF) was used at 200 kV to characterize the morphology and the particle size distribution of the synthesized products. The samples were prepared by suspending them in ethanol and dispersing them by sonication. A drop of the solution was poured onto a copper-grid-supported carbon film. Then, the grid was dried in air prior to observation.

Catalytic Measurements. *Oxygen Reduction Reaction (ORR).* Electrochemical measurements were carried out by cyclic voltammetry (CV) on a CHI 660B electrochemical workstation. A conventional, three-electrode cell consisting of glassy carbon electrode (GCE) with an area of 0.125 cm^2 was used as the working electrode, Pt foil was employed as the counter electrode and Hg/HgO (0.1 M KOH) (MMO, 0.098 V *vs* SHE) was used as the reference electrode. All potentials were referenced to a reversible hydrogen electrode (RHE) by adding a value of (0.098 + 0.059 × pH) V. The working electrode was modified with a catalyst layer by dropping a suitable amount of catalyst ink on the GCE. The catalyst ink was prepared by ultrasonically dispersing 1.0 mg of the carbon supported catalysts in a 1.0 mL solution (0.9 mL of ethanol and 0.1 mL of 5 wt % Nafion solution) for 30 min to obtain a homogeneous solution. Ten microliters of the dispersion was pipetted out and dropped onto a glassy carbon rotating disk electrode of 3 mm in diameter, which was then dried in air. CV experiments were conducted at room temperature in 0.1 M KOH solution saturated with nitrogen. For all of the experiments, stable voltammogram curves were recorded after scanning for 20 cycles in the potential region from 0 to 0.6 V in 0.1 M KOH solution. Polarization curves for the oxygen reduction reaction (ORR) were obtained in 0.1 M KOH solution using the rotating disk electrode. Before the RDE study, the electrodes were cycled at 50 mV s^{-1} between 0 and 0.6 V until reproducible cyclic voltammograms were obtained. Normalized currents are given in terms of geometric weight (mA cm^{-2}). The working electrode was scanned cathodically at a rate of 5 mV s^{-1} with varying rotating speed from 225 to 2025 rpm. Koutecky−Levich plots (J^{-1} *vs* $\omega^{-1/2}$) were analyzed at various electrode potentials. The slopes of their best linear fit lines were used to calculate the number of electrons transferred (n) on the basis of the Koutecky−Levich equation:

$$\frac{1}{J} = \frac{1}{J_k} + \frac{1}{J_L} = \frac{1}{J_k} + \frac{1}{B\omega^{1/2}} \quad (1)$$

$$B = 0.62nFC_0D_0^{2/3}\gamma^{-1/6} \quad (2)$$

$$J_k = nFkC_0 \quad (3)$$

where J is the measured current density, J_k and J_L are the kinetic- and diffusion-limiting current densities, ω is the angular velocity, n is transferred electron number, F is the Faraday constant (96 485 C mol^{-1}), C_0 is the bulk concentration of O_2 (1.2×10^{-6} mol cm^{-3}), ν is the kinematic viscosity of the electrolyte (0.01 cm^2 s^{-1}), D_0 is the O_2 diffusion coefficient (1.9×10^{-5} cm^2 s^{-1}), and k is the electron-transfer rate constant. The number of electrons transferred (n) and J_k can be obtained from the slope and intercept of the Koutecky−Levich plots, respectively.

Hydrogen Evolution Reaction (HER). The HER activity of various M_3C-GNRs (M: Fe, Co, Ni) hybrids was performed in argon-purged 0.5 M H_2SO_4 at room temperature using a standard three-electrode setup. A Pt foil (100% Pt, 5 × 10 mm, SPI Supplies, West Chester, PA) was used as the counter electrode. The acquired currents were tentatively normalized by the surface area calculated from the Levich analysis. Ag-AgCl (4 M AgCl-KCl) was used as the reference electrode. All potentials were referenced to a reversible hydrogen electrode (RHE) by adding a value of (0.2415 + 0.059 × pH) V. Prior to all measurements, the electrochemical cell was bubbled for 30 min with H_2. To condition the electrodes, 25 CV cycles were conducted between 0.0 V (*vs* the normal hydrogen electrode, NHE) and the onset of oxidation at 50 mV s^{-1}. Tafel curves were then obtained from linear sweep voltammograms using a scan rate of 50 mV s^{-1}. Homogeneity of the platinum-modified surfaces was confirmed by the observation of uniform H_2 gas evolution from the electrode surfaces.

Roughness Factor Calculation. The electrochemically active surface area (EASA) was estimated from the electrochemical double-layer capacitance of the nanoporous layers. The double layer capacitance (C_{dl}) was determined with a simple cyclic voltammetry (CV) method. The EASA is then calculated from the double-layer capacitance according to

$$\text{EASA} = \frac{C_{dl}}{C_s} \quad (4)$$

where C_s is the capacitance of an atomically smooth planar surface of the material per unit area under identical electrolyte conditions. An average value of $C_s = 22\ \mu$F cm^{-2} is used in this work. The roughness factor (RF) is then calculated by dividing the estimated EASA by the geometric area of the electrode.

Conflict of Interest: The authors declare no competing financial interest.

Acknowledgment. The authors acknowledge Prof. James M. Tour and Dr. Robert H. Hauge at Rice University for providing research facilities, helpful discussions and assistance, Yang Yang, Gedeng Ruan, Huilong Fei, Lei Li, and Jian Lin for helpful discussions, and the China Scholarship Council for partial support of this research.

Supporting Information Available: Materials, M_3C (M: Fe, Co, Ni) nanocrystals synthesis and characterizations, and their electrochemical measurements; Tables S1 and S2; Figures S1−S16. The Supporting Information is available free of charge on the ACS Publications website at DOI: 10.1021/acsnano.5b02420.

REFERENCES AND NOTES

1. Srivastava, R.; Mani, P.; Hahn, N.; Strasser, P. Efficient Oxygen Reduction Fuel Cell Electrocatalysis on Voltammetrically Dealloyed Pt−Cu−Co Nanoparticles. *Angew. Chem.* **2007**, *119*, 9146–9149.
2. Xie, J.; Zhang, J.; Li, S.; Grote, F.; Zhang, X.; Zhang, H.; Wang, R.; Lei, Y.; Pan, B.; Xie, Y. Controllable Disorder Engineering in Oxygen-Incorporated MoS_2 Ultrathin Nanosheets for Efficient Hydrogen Evolution. *J. Am. Chem. Soc.* **2013**, *135*, 17881–17888.
3. Esposito, D. V.; Hunt, S. T.; Kimmel, Y. C.; Chen, J. G. A New Class of Electrocatalysts for Hydrogen Production from Water Electrolysis: Metal Monolayers Supported on Low-Cost Transition Metal Carbides. *J. Am. Chem. Soc.* **2012**, *134*, 3025–3033.
4. Greeley, J.; Stephens, I.; Bondarenko, A.; Johansson, T. P.; Hansen, H. A.; Jaramillo, T.; Rossmeisl, J.; Chorkendorff, I.; Nørskov, J. K. Alloys of Platinum and Early Transition Metals as Oxygen Reduction Electrocatalysts. *Nat. Chem.* **2009**, *1*, 552–556.
5. Lim, B.; Jiang, M.; Camargo, P. H. C.; Cho, E. C.; Tao, J.; Lu, X.; Zhu, Y.; Xia, Y. Pd-Pt Bimetallic Nanodendrites with High Activity for Oxygen Reduction. *Science* **2009**, *324*, 1302–1305.
6. Wang, H.; Lu, Z.; Kong, D.; Sun, J.; Hymel, T. M.; Cui, Y. Electrochemical Tuning of MoS_2 Nanoparticles on Three-Dimensional Substrate for Efficient Hydrogen Evolution. *ACS Nano* **2014**, *8*, 4940–4947.
7. Shi, J.; Ma, D.; Han, G.-F.; Zhang, Y.; Ji, Q.; Gao, T.; Sun, J.; Song, X.; Li, C.; Zhang, Y.; et al. Controllable Growth and Transfer of Monolayer MoS_2 on Au Foils and Its Potential Application in Hydrogen Evolution Reaction. *ACS Nano* **2014**, *8*, 10196–10204.
8. Li, Y.; Wang, H.; Xie, L.; Liang, Y.; Hong, G.; Dai, H. MoS_2 Nanoparticles Grown on Graphene: An Advanced Catalyst for the Hydrogen Evolution Reaction. *J. Am. Chem. Soc.* **2011**, *133*, 7296–7299.
9. Kong, D.; Wang, H.; Lu, Z.; Cui, Y. $CoSe_2$ Nanoparticles Grown on Carbon Fiber Paper: An Efficient and Stable Electrocatalyst for Hydrogen Evolution Reaction. *J. Am. Chem. Soc.* **2014**, *136*, 4897–4900.
10. Cheng, L.; Huang, W.; Gong, Q.; Liu, C.; Liu, Z.; Li, Y.; Dai, H. Inside Back Cover: Ultrathin WS2 Nanoflakes as a High-Performance Electrocatalyst for the Hydrogen Evolution Reaction. *Angew. Chem., Int. Ed.* **2014**, *53*, 7957–7957.
11. Garcia-Esparza, A. T.; Cha, D.; Ou, Y.; Kubota, J.; Domen, K.; Takanabe, K. Tungsten Carbide Nanoparticles as Efficient Cocatalysts for Photocatalytic Overall Water Splitting. *ChemSusChem* **2013**, *6*, 168–181.
12. Xu, K.; Wang, F.; Wang, Z.; Zhan, X.; Wang, Q.; Cheng, Z.; Safdar, M.; He, J. Component-Controllable $WS_{2(1-x)}Se_{2x}$ Nanotubes for Efficient Hydrogen Evolution Reaction. *ACS Nano* **2014**, *8*, 8468–8476.
13. Youn, D. H.; Han, S.; Kim, J. Y.; Kim, J. Y.; Park, H.; Choi, S. H.; Lee, J. S. Highly Active and Stable Hydrogen Evolution Electrocatalysts Based on Molybdenum Compounds on Carbon Nanotube−Graphene Hybrid Support. *ACS Nano* **2014**, *8*, 5164–5173.
14. Liao, L.; Bian, X.; Xiao, J.; Liu, B.; Scanlon, M. D.; Girault, H. H. Nanoporous Molybdenum Carbide Wires as an Active Electrocatalyst towards the Oxygen Reduction Reaction. *Phys. Chem. Chem. Phys.* **2014**, *16*, 10088–10094.
15. Chen, W. F.; Wang, C. H.; Sasaki, K.; Marinkovic, N.; Xu, W.; Muckerman, J. T.; Zhu, Y.; Adzic, R. R. Highly Active and Durable Nanostructured Molybdenum Carbide Electrocatalysts for Hydrogen Production. *Energy Environ. Sci.* **2013**, *6*, 943–951.
16. Callejas, J. F.; McEnaney, J. M.; Read, C. G.; Crompton, J. C.; Biacchi, A. J.; Popczun, E. J.; Gordon, T. R.; Lewis, N. S.; Schaak, R. E. Electrocatalytic and Photocatalytic Hydrogen Production from Acidic and Neutral-pH Aqueous Solutions Using Iron Phosphide Nanoparticles. *ACS Nano* **2014**, *8*, 11101–11107.
17. Xu, Y.; Wu, R.; Zhang, J.; Shi, Y.; Zhang, B. Anion-Exchange Synthesis of Nanoporous FeP Nanosheets as Electrocatalysts for Hydrogen Evolution Reaction. *Chem. Commun.* **2013**, *49*, 6656–6658.
18. Liu, Q.; Tian, J.; Cui, W.; Jiang, P.; Cheng, N.; Asiri, A. M.; Sun, X. Carbon Nanotubes Decorated with CoP Nanocrystals: A Highly Active Non-Noble-Metal Nanohybrid Electrocatalyst for Hydrogen Evolution. *Angew. Chem., Int. Ed.* **2014**, *53*, 6710–6714.
19. Popczun, E. J.; McKone, J. R.; Read, C. G.; Biacchi, A. J.; Wiltrout, A. M.; Lewis, N. S.; Schaak, R. E. Nanostructured Nickel Phosphide as an Electrocatalyst for the Hydrogen Evolution Reaction. *J. Am. Chem. Soc.* **2013**, *135*, 9267–9270.
20. Chen, W. F.; Sasaki, K.; Ma, C.; Frenkel, A. I.; Marinkovic, N.; Muckerman, J. T.; Zhu, Y.; Adzic, R. R. Hydrogen-Evolution Catalysts Based on Non-Noble Metal Nickel−Molybdenum Nitride Nanosheets. *Angew. Chem., Int. Ed.* **2012**, *51*, 6131–6135.
21. Wu, G.; More, K. L.; Johnston, C. M.; Zelenay, P. High-Performance Electrocatalysts for Oxygen Reduction Derived from Polyaniline, Iron, and Cobalt. *Science* **2011**, *332*, 443–447.
22. Zou, X.; Huang, X.; Goswami, A.; Silva, R.; Sathe, B. R.; Mikmeková, E.; Asefa, T. Cobalt-Embedded Nitrogen-Rich Carbon Nanotubes Efficiently Catalyze Hydrogen Evolution Reaction at All pH Values. *Angew. Chem., Int. Ed.* **2014**, *53*, 4372–4376.
23. Lefèvre, M.; Proietti, E.; Jaouen, F.; Dodelet, J.-P. Iron-based Catalysts with Improved Oxygen Reduction Activity in Polymer Electrolyte Fuel Cells. *Science* **2009**, *324*, 71–74.
24. Shao, M.-H.; Sasaki, K.; Adzic, R. R. Pd-Fe Nanoparticles as Electrocatalysts for Oxygen Reduction. *J. Am. Chem. Soc.* **2006**, *128*, 3526–3527.
25. Kleiman-Shwarsctein, A.; Hu, Y.-S.; Forman, A. J.; Stucky, G. D.; McFarland, E. W. Electrodeposition of α-Fe_2O_3 Doped with Mo or Cr as Photoanodes for Photocatalytic Water Splitting. *J. Phys. Chem. C* **2008**, *112*, 15900–15907.
26. Wu, Z.-S.; Yang, S.; Sun, Y.; Parvez, K.; Feng, X.; Müllen, K. 3D Nitrogen-Doped Graphene Aerogel-Supported Fe_3O_4 Nanoparticles as Efficient Electrocatalysts for the Oxygen Reduction Reaction. *J. Am. Chem. Soc.* **2012**, *134*, 9082–9085.
27. Wang, C.; Daimon, H.; Sun, S. Dumbbell-like Pt− Fe_3O_4 Nanoparticles and Their Enhanced Catalysis for Oxygen Reduction Reaction. *Nano Lett.* **2009**, *9*, 1493–1496.
28. Liang, Y.; Li, Y.; Wang, H.; Zhou, J.; Wang, J.; Regier, T.; Dai, H. Co_3O_4 Nanocrystals on Graphene as a Synergistic Catalyst for Oxygen Reduction Reaction. *Nat. Mater.* **2011**, *10*, 780–786.
29. Takasu, Y.; Yoshinaga, N.; Sugimoto, W. Oxygen Reduction Behavior of RuO_2/Ti, IrO_2/Ti and IrM (M: Ru, Mo, W, V)O_x/Ti Binary Oxide Electrodes in a Sulfuric Acid Solution. *Electrochem. Commun.* **2008**, *10*, 668–672.
30. Xie, J.; Zhang, H.; Li, S.; Wang, R.; Sun, X.; Zhou, M.; Zhou, J.; Lou, X. W.; Xie, Y. Defect-Rich MoS_2 Ultrathin Nanosheets with Additional Active Edge Sites for Enhanced Electrocatalytic Hydrogen Evolution. *Adv. Mater.* **2013**, *25*, 5807–5813.
31. Hu, Y.; Jensen, J. O.; Zhang, W.; Cleemann, L. N.; Xing, W.; Bjerrum, N. J.; Li, Q. Hollow Spheres of Iron Carbide Nanoparticles Encased in Graphitic Layers as Oxygen Reduction Catalysts. *Angew. Chem., Int. Ed.* **2014**, *53*, 3675–3679.
32. Hou, Y.; Huang, T.; Wen, Z.; Mao, S.; Cui, S.; Chen, J. Metal−Organic Framework-Derived Nitrogen-Doped Core-Shell-Structured Porous Fe/Fe_3C@C Nanoboxes Supported on Graphene Sheets for Efficient Oxygen Reduction Reactions. *Adv. Energy Mater.* **2014**, *4*, 1400337.
33. Xu, P.; Han, X. J.; Liu, X. R.; Zhang, B.; Wang, C.; Wang, X. H. A Study of the Magnetic and Electromagnetic Properties of γ-Fe_2O_3−Multiwalled Carbon Nanotubes (MWCNT) and

Fe/Fe_3C−MWCNT Composites. *Mater. Chem. Phys.* **2009**, *114*, 556–560.
34. López de Arroyabe Loyo, R.; Loyo, R.; Nikitenko, S. I.; Scheinost, A. C.; Simonoff, M. Immobilization of Selenite on Fe_3O_4 and Fe/Fe_3C Ultrasmall Particles. *Environ. Sci. Technol.* **2008**, *42*, 2451–2456.
35. Leslie-Pelecky, D. L.; Zhang, X.; Kim, S.; Bonder, M.; Rieke, R. D. Structural Properties of Chemically Synthesized Nanostructured Ni and Ni: Ni_3C Nanocomposites. *Chem. Mater.* **1998**, *10*, 164–171.
36. Wen, Z.; Ci, S.; Zhang, F.; Feng, X.; Cui, S.; Mao, S.; Luo, S.; He, Z.; Chen, J. Nitrogen-Enriched Core-Shell Structured Fe/Fe_3C-C Nanorods as Advanced Electrocatalysts for Oxygen Reduction Reaction. *Adv. Mater.* **2012**, *24*, 1399–1404.
37. Carroll, K. J.; Huba, Z. J.; Spurgeon, S. R.; Qian, M.; Khanna, S. N.; Hudgins, D. M.; Taheri, M. L.; Carpenter, E. E. Magnetic Properties of Co_2C and Co_3C Nanoparticles and Their Assemblies. *Appl. Phys. Lett.* **2012**, *101*, 012409.
38. Zhou, W.; Zheng, K.; He, L.; Wang, R.; Guo, L.; Chen, C.; Han, X.; Zhang, Z. Ni/Ni_3C Core−Shell Nanochains and Its Magnetic Properties: One-Step Synthesis at Low Temperature. *Nano Lett.* **2008**, *8*, 1147–1152.
39. Lee, H. J.; Cho, W.; Lim, E.; Oh, M. One-pot Synthesis of Magnetic Particle-embedded Porous Carbon Composites from Metal-organic Frameworks and Their Sorption Properties. *Chem. Commun.* **2014**, *50*, 5476–5479.
40. Nikitenko, S. I.; Koltypin, Y.; Palchik, O.; Felner, I.; Xu, X. N.; Gedanken, A. Synthesis of Highly Magnetic, Air-Stable Iron−Iron Carbide Nanocrystalline Particles by Using Power Ultrasound. *Angew. Chem.* **2001**, *113*, 4579–4581.
41. Dong, X. L.; Zhang, Z. D.; Xiao, Q. F.; Zhao, X. G.; Chuang, Y. C.; Jin, S. R.; Sun, W. M.; Li, Z. J.; Zheng, Z. X.; Yang, H. Characterization of ultrafine γ-Fe(C), α-Fe(C) and Fe_3C Particles Synthesized by Arc-discharge in Methane. *J. Mater. Sci.* **1998**, *33*, 1915–1919.
42. Yang, W.; Liu, X.; Yue, X.; Jia, J.; Guo, S. Bamboo-like Carbon Nanotube/Fe_3C Nanoparticle Hybrids and Their Highly Efficient Catalysis for Oxygen Reduction. *J. Am. Chem. Soc.* **2015**, *137*, 1436–1439.
43. Deng, J.; Ren, P.; Deng, D.; Bao, X. Enhanced Electron Penetration through an Ultrathin Graphene Layer for Highly Efficient Catalysis of the Hydrogen Evolution Reaction. *Angew. Chem., Int. Ed.* **2015**, *54*, 2100–2104.
44. Deng, J.; Ren, P.; Deng, D.; Yu, L.; Yang, F.; Bao, X. Highly Active and Durable Non-precious-metal Catalysts Encapsulated in Carbon Nanotubes for Hydrogen Evolution Reaction. *Energy Environ. Sci.* **2014**, *7*, 1919–1923.
45. Lee, C.; Wei, X.; Kysar, J. W.; Hone, J. Measurement of the Elastic Properties and Intrinsic Strength of Monolayer Graphene. *Science* **2008**, *321*, 385–388.
46. Fan, X.; Peng, Z.; Yang, Y.; Zhou, H.; Guo, X. Atomic H-induced Cutting and Unzipping of Single-Walled Carbon Nanotube Carpets with Teepee Structure and Their Enhanced Supercapacitor Performance. *J. Mater. Chem. A* **2015**, *3*, 10077–10084.
47. Lee, J.-S.; Park, G. S.; Kim, S. T.; Liu, M.; Cho, J. A Highly Efficient Electrocatalyst for the Oxygen Reduction Reaction: N-Doped Ketjenblack Incorporated into Fe/Fe_3C-Functionalized Melamine Foam. *Angew. Chem., Int. Ed.* **2013**, *52*, 1026–1030.
48. Fan, X.; Zhou, H.; Guo, X. WC Nanocrystals Grown on Vertically Aligned Carbon Nanotubes: An Efficient and Stable Electrocatalyst for Hydrogen Evolution Reaction. *ACS Nano* **2015**, *9*, 5125–5134.
49. Wang, C.; Gao, H.; Chen, X.; Yuan, W. Z.; Zhang, Y. Enabling Carbon Nanofibers with Significantly Improved Graphitization and Homogeneous Catalyst Deposition for High Performance Electrocatalysts. *Electrochim. Acta* **2015**, *152*, 383–390.
50. Parvez, K.; Yang, S.; Hernandez, Y.; Winter, A.; Turchanin, A.; Feng, X.; Müllen, K. Nitrogen-Doped Graphene and Its Iron-Based Composite As Efficient Electrocatalysts for Oxygen Reduction Reaction. *ACS Nano* **2012**, *6*, 9541–9550.
51. Zhang, H.; Liang, C.; Liu, J.; Tian, Z.; Shao, G. The Formation of Onion-like Carbon-Encapsulated Cobalt Carbide Core/Shell Nanoparticles by the Laser Ablation of Metallic Cobalt in Acetone. *Carbon* **2013**, *55*, 108–115.
52. Yang, C.; Zhao, H.; Hou, Y.; Ma, D. Fe_5C_2 Nanoparticles: A Facile Bromide-Induced Synthesis and as an Active Phase for Fischer−Tropsch Synthesis. *J. Am. Chem. Soc.* **2012**, *134*, 15814–15821.
53. Yang, W.; Miao, H.; Xie, Z.; Zhang, L.; An, L. Synthesis of Silicon Carbide Nanorods by Catalyst-Assisted Pyrolysis of Polymeric Precursor. *Chem. Phys. Lett.* **2004**, *383*, 441–444.
54. Lin, L.; Zhu, Q.; Xu, A.-W. Noble-Metal-Free Fe−N/C Catalyst for Highly Efficient Oxygen Reduction Reaction under Both Alkaline and Acidic Conditions. *J. Am. Chem. Soc.* **2014**, *136*, 11027–11033.
55. McCrory, C. C. L.; Jung, S.; Peters, J. C.; Jaramillo, T. F. Benchmarking Heterogeneous Electrocatalysts for the Oxygen Evolution Reaction. *J. Am. Chem. Soc.* **2013**, *135*, 16977–16987.